Title
Phasor S-FLIM: a new paradigm for fast and robust spectral fluorescence lifetime imaging

Journal
Nature Methods, 18(5)

ISSN
1548-7091

Authors
Scipioni, Lorenzo
Rossetta, Alessandro
Tedeschi, Giulia
et al.

Publication Date
2021-05-01

DOI
10.1038/s41592-021-01108-4

Peer reviewed

HHS Public Access

Author manuscript

Nat Methods. Author manuscript; available in PMC 2023 May 05.

Published in final edited form as:

Nat Methods. 2021 May ; 18(5): 542–550. doi:10.1038/s41592-021-01108-4.

Phasor S-FLIM: a new paradigm for fast and robust spectral fluorescence lifetime imaging

Lorenzo Scipioni[1], **Alessandro Rossetta**[2], **Giulia Tedeschi**[1], **Enrico Gratton**[1,✉]

[1]Laboratory for Fluorescence Dynamics, Biomedical Engineering Department, University of California, Irvine, CA, USA.

[2]FLIM LABS, Rome, Italy.

Abstract

Fluorescence lifetime imaging microscopy (FLIM) and spectral imaging are two broadly applied methods for increasing dimensionality in microscopy. However, their combination is typically inefficient and slow in terms of acquisition and processing. By integrating technological and computational advances, we developed a robust and unbiased spectral FLIM (S-FLIM) system. Our method, Phasor S-FLIM, combines true parallel multichannel digital frequency domain electronics with a multidimensional phasor approach to extract detailed and precise information about the photophysics of fluorescent specimens at optical resolution. To show the flexibility of the Phasor S-FLIM technology and its applications to the biological and biomedical field, we address four common, yet challenging, problems: the blind unmixing of spectral and lifetime signatures from multiple unknown species, the unbiased bleedthrough- and background-free Förster resonance energy transfer analysis of biosensors, the photophysical characterization of environment-sensitive probes in living cells and parallel four-color FLIM imaging in tumor spheroids.

Obtaining reliable FLIM data from cellular samples can prove to be a challenging task. The main difficulties arise from the need for obtaining a high number of photons per pixel (efficient optics and electronics) and the presence of complex fluorescence decays at each pixel (efficient processing and analysis). The relatively low photon yield in tissue

✉**Correspondence and requests for materials** should be addressed to E.G., egratton22@gmail.com.

Author contributions

L.S. and E.G. conceived the idea. A.R. developed and wrote FPGA code. L.S., A.R. and E.G. wrote code. L.S. designed electronics, built the microscope and performed simulations and experiments. G.T. prepared all biological samples. L.S. wrote the paper with input from all authors

Competing interests

A.R. declares his involvement in FLIM LABS Srl, Rome, Italy.

Reporting Summary. Further information on research design is available in the Nature Research Reporting Summary linked to this article.

Code availability

The code for performing blind unmixing is provided, together with a script for simulating S-FLIM data for testing and an example of experimental S-FLIM data. Further code is available from the corresponding author upon reasonable request.

Additional information

Supplementary information The online version contains supplementary material available at https://doi.org/10.1038/s41592-021-01108-4.

and cellular samples is worsened by the need for narrow filters for multicolor experiments and the presence of unknown background (for example, autofluorescence). Moreover, the presence of complex decays (for example, multi-exponential decays, rise time, uncorrelated background and instrument response function (IRF) convolution) results in the need for increasing the number of fitting parameters and selecting a fitting model a priori.

In recent years, several microscope implementations that can provide lifetime and spectral information simultaneously have been developed. These systems usually rely on either time correlated single photon counting[1] or gated optical intensifiers[2] technologies as methods for obtaining the lifetime information. These techniques use either a detector array[3] or multiple single detectors[4] to obtain the emission spectrum information. However, despite the many advancements that have been achieved using parallel detectors from both a technological (detectors and electronics) and a computational (acquisition and postprocessing) point of view, very few S-FLIM technologies are commercially available due to the high cost, the limited performances and the need for dedicated electronics and/or software. Current S-FLIM technologies are carried out either with limited spectral resolution or sequentially[4], therefore greatly decreasing the number of photons collected as well as the acquisition speed. The simultaneous measurement in a true parallel configuration of several spectral and lifetime channels over the entire visible range has not been exploited so far and can have applications in many areas of biology and medicine[5–8].

To overcome these challenges, we developed Phasor S-FLIM, a method that combines the true parallel, simultaneous lifetime and spectral detection with phasor analysis to obtain fast, unbiased, high-precision FLIM data that can be processed in real time. Our Phasor S-FLIM implementation features a photomultiplier tube (PMT) detector array that can provide simultaneously spectral and lifetime information on 32 independent channels, detecting wavelengths ranging from 404 to 670 nm, coupled with a new multichannel digital frequency domain- (DFD)-based electronics setup. The data are then processed by an original phasor-based blind unmixing algorithm.

The approach presented in this work can retrieve both the spectral and lifetime signature from an unknown mixture of fluorophores, as we demonstrate through simulations and solution data as well as with live and fixed cells labeled with a series of fluorescent dyes. The capability to obtain unbiased spectral and lifetime information without a priori knowledge is particularly important in the case of fluorescence resonance energy transfer (FRET) and, specifically, with FRET-based biosensors that require low expression levels and therefore yield a weak fluorescence signal. Using Phasor S-FLIM it is possible to simultaneously account for detrimental contributions (for example, background and autofluorescence) as well as unmixing both donor and acceptor lifetime to obtain a robust and photon-efficient multiparametric determination of the FRET efficiency. Finally, the simultaneous access to spectral and lifetime information allows for an in-depth characterization of dyes that change their photophysical signature according to environmental conditions. Specifically, we show that by labeling tumor spheroids with environment-sensitive dyes and by acquiring and processing the data with Phasor S-FLIM, it is possible to achieve fast four-color FLIM and combine the fluorescence information to spatially map a series of metabolic parameters of interest.

Results

The phasor approach and the DFD.

The workflow of our Phasor S-FLIM system is described in Fig. 1a and more in detail in the Supplementary Information. In our setup, we use a custom-made confocal microscope (Supplementary Fig. 1), equipped with a 78 MHz pulsed white light laser that is successively divided into four parallel and independent laser lines (405, 488, 561, 647 nm). The fluorescence is separated by color by a diffraction grating and collected by a 32-channel PMT array, the output of each detector is sent to two 16 channels constant fraction discriminators (CFDs), processed by a field-programmable gate array (FPGA) programmed following the DFD[9–11] principle and data are streamed via USB 3.0 to a computer for processing. Data processing exploits a phasor-based blind unmixing algorithm that relies on the analysis of the lifetime phasors for each of the spectral channels to obtain the pure spectral and subsequently lifetime signature of the species that compose the system.

S-FLIM alone is already a powerful technique, but the large amount of data and the inevitable overlapping of spectral emissions from multiple species requires a fast and precise analysis to make the method more broadly applicable and accessible. For this reason, we coupled our S-FLIM system to a new phasor-based processing and unmixing algorithm that is meant to provide real-time analysis and blind unmixing of the S-FLIM dataset.

The phasor approach[12] (Supplementary Fig. 3) for the analysis of FLIM datasets was introduced over a decade ago and it has found extensive applications[11,13–15] because of its use in terms of easiness of implementation, speed and the immediate graphical representation of FLIM data. The approach has been extended more recently to the analysis of spectral signals[16–19] and relies on the same principle and mathematics.

The main advantages in the use of the phasor approach in an S-FLIM context are summarized in Fig. 1. FLIM images are typically composed of a few hundreds of photons per pixel at best, which results in undersampled lifetime curves. Undersampling results in a bias in the fitting procedure that skews the results when the number of photons is low (Fig. 1b), however, the bias is much less prominent if the same data are analyzed with the phasor approach, which is also slightly more precise (Fig. 1c) and over two orders of magnitude faster (Fig. 1d) at obtaining the lifetime of a single exponential decay only affected by Poissonian noise. However, microscopy data are affected by a number of other detrimental factors, such as the IRF, which decreases the temporal resolution and detector dark noise, which results in decreased signal-to-background ratio (SBR). For this reason, we simulated a series of Gaussian IRFs with varying FWHM (full-width at half-maximum) values and increasing the contribution of SBR, shown as the ratio of number of decay pho tons over the number of background photons (Fig. 1e–j). Again, the phasor approach shows increased precision (Fig. 1f,i), decreased bias (Fig. 1e,h) and a three orders of magnitude lower execution time (Fig. 1g,j) with respect to the least mean square (LMS) fitting procedure, making it ideal for the real-time analysis of FLIM images.

In our system, lifetime information is sampled in 256 bins and the execution time for transforming a S-FLIM dataset (256 × 256 × 256 × 32) is approximately 3.5 s

(approximately 64 μs per pixel), which is further reduced to 1.5 ms (<1 μs per pixel), by exploiting graphics processing unit acceleration.

From an electronic point of view, the timing architecture has to be perfectly linear throughout the entire laser period, which is not always the case with traditional time correlated single photon counting implementations[20] (Supplementary Information). The use of DFD has the advantage that the bins of the fluorescence decay histogram are always a submultiple of the laser frequency. Therefore, when converting such a histogram into phasors, no error propagates within the mathematical operation, whereas several parameters have to be taken into consideration when using the time-domain decay[20] and they rely on a priori knowledge of the lifetime decays present in the sample, which is not always available. Furthermore, DFD uses considerably fewer resources in a FPGA, which gives a higher scalability and potential for highly parallel systems (Supplementary Information).

Spectral and lifetime blind unmixing of three unknown components.

Spectral unmixing[21–24] is a well-studied method applied to a wide range of problems and can be applied blindly or with a priori knowledge about the spectral emission of the underlying species. Most of the implementations of blind unmixing rely on the assumption that at least one pixel of the image carries the information of a pure species that, in biological samples, is rarely applicable, especially in the presence of a variable or unknown background. By exploiting the simultaneous acquisition of spectral and lifetime information, we show that our Phasor S-FLIM unmixing algorithm can also be applied to few, or even single pixels, regardless of any assumptions of pixels containing a pure species.

Let us assume we have a function of interest $I(x)$, which is a linear combination of three species $I(x) = f_1 I_1(x) + f_2 I_2(x) + f_3 I_3(x)$, where f_1, f_2 and f_3 are the fractions for the total number of photons yielded by that species with the constraint that their sum equals one ($f_1 + f_2 + f_3 = 1$). Once transformed into phasor space, $I(x)$ will be represented by a point inside a triangle, the vertices of which are constituted by the phasors of its pure species $I_1(x)$, $I_2(x)$ and $I_3(x)$ (Supplementary Fig. 3). This phasor's property has been previously exploited to implement phasor-based spectral unmixing given the spectral profile of the pure species (or their positions in the phasor space).

An S-FLIM image is a multidimensional array $XYTS$, where X and Y are the spatial dimensions, T represents the nanosecond decay time and S represents the spectral dimension. For simplicity, we can consider only the $T \times S$ matrix $I(t, \lambda)$, where lifetime is sampled in m points ($t = t_1, \ldots, t_m$) and the spectral dimension is sampled in n points ($\lambda = \lambda_1, \ldots, \lambda_n$). This matrix is called time-resolved emission spectrum (TRES) or time-resolved area-normalized emission spectrum (TRANES[25,26]) if the spectral emission at every temporal point is normalized so that the sum equals one.

The workflow of our algorithm is described below and a schematic representation is provided in Fig. 1a and more in detail in Supplementary Fig. 7. In the following, the phasor coordinates obtained by transforming the temporal dimension will be defined by $\left(g^{(\tau)}, s^{(\tau)}\right)$

and called τ phasors, whereas the phasor coordinates obtained by transforming the spectral dimension will be defined by $\left(g^{(\lambda)}, s^{(\lambda)}\right)$ and called λ phasors.

1. The TRES matrix $I(t, \lambda)$ is transformed into τ phasors, obtaining a set of n coordinates $\left(g^{(\tau)}(\lambda), s^{(\tau)}(\lambda)\right)$, each of which carries a different and unknown weight for each of the pure species.
2. The $\left(g^{(\tau)}(\lambda), s^{(\tau)}(\lambda)\right)$ coordinates are transformed by means of principal component analysis (PCA) to find the direction of maximum variance, then the coordinates are rotated by 45° to have equal variance for each dimension, obtaining the coordinates $\left(g^{(\tau)'}(\lambda), s^{(\tau)'}(\lambda)\right)$. Note that PCA is only used for variance maximization and not for the determination of the end-members. The coordinates will be successively back transformed to the native space.
3. $\left(g^{(\tau)'}(\lambda), s^{(\tau)'}(\lambda)\right)$ are fitted with a double generalized logistic function (Supplementary Fig. 8 and Supplementary Information) to obtain the pure species (end-members) in the PCA-transformed coordinates, which are then back transformed to obtain the positions of the pure lifetime components $\left(g_1^{(\tau)}, s_1^{(\tau)}\right)$, $\left(g_2^{(\tau)}, s_2^{(\tau)}\right)$ and $\left(g_3^{(\tau)}, s_3^{(\tau)}\right)$ (Fig. 1a and Supplementary Figs 9 and 10, empty circles).
4. Using the retrieved pure τ-phasor coordinates, we obtain the fractions $f_1^{(\tau)}(\lambda)$, $f_2^{(\tau)}(\lambda)$ and $f_3^{(\tau)}(\lambda)$ from which, by element-wise multiplication with the steady-state spectrum, we can obtain the unmixed spectra of the three underlying components (Fig. 1, top right).
5. Once retrieved the unmixed spectra, we then transform each of them in the λ-phasor space, obtaining the three pure $\left(g^{(\lambda)}, s^{(\lambda)}\right)$ components that will be used to unmix each point in the temporal dimension and calculate the fractions $f_1^{(\lambda)}(t)$, $f_2^{(\lambda)}(t)$ and $f_3^{(\lambda)}(t)$.
6. Similar to point 4, the temporal dimension is unmixed in the three underlying lifetime components (Fig. 1, bottom right), completing the Phasor S-FLIM blind unmixing algorithm.

To test the algorithm, a simulation (Supplementary Fig. 9) was carried out with 500,000 photons in total, which corresponds to an S-FLIM image of approximately 7.6 photons per pixel (2.5 photons per species per pixel), a weak fluorescence signal. Two of the lifetime decays were simulated as multi-exponential decays, to show that no a priori knowledge of the functional form of the decay is needed to successfully carry out the Phasor S-FLIM unmixing algorithm. The algorithm requires the species to have distinct spectral and lifetime signatures; however, they can be as close as 200 ps and 20 nm for two components (Supplementary Fig. 12) or 400 ps and 32 nm for three components (Supplementary Fig. 13). To validate the algorithm in nonsimulated samples, we tested it experimentally on a mixture of three fluorophores (Alexa 405, SeTau 405 and ATTO 490 LS) and compared the unmixed spectra and lifetime decays with the corresponding curves of the single solutions (Supplementary Fig. 10), showing a precise recovery of both spectral and lifetime

information (Supplementary Table 1). No spectral correction has been applied to any of the datasets presented in this paper.

To further explore the algorithm potential in cellular samples, we tested it in fluorescently labeled live and fixed cells, exciting them at 488 nm and recording the fluorescence over 18 spectral channels (Fig. 2).

Despite the reduced number of spectral channels, the algorithm correctly retrieves spectral and lifetime information in both live (Fig. 2a,b) and fixed (Fig. 2c–f) cells, even with a very low number of photons (0.6 photons per pixel per dye) in structured samples. Note that the unmixing procedures achieved in Fig. 2 are not possible to obtain using emission filters, since the emission wavelengths for MitoTracker Orange and LysoTracker Red differ by as little as 14 nm (Fig. 2b) and the anti-TOMM20/Alexa555 antibody emits over ten times higher the number of photons of the Phalloidin-Alexa564 (Fig. 2c–f). Moreover, the median execution time, computed on 1,000 replicates, for the unmixing algorithm is approximately 100 ms, meaning that it could be applied in real time during the acquisition and, in contrast with other blind unmixing methods relying on phasors[27], it only exploits the first harmonic of the phasor transformation, which is the least affected by noise.

Phasor S-FLIM unmixing as a new paradigm for FRET.

In the following, we will demonstrate that the combination of Phasor S-FLIM with the blind unmixing algorithm presented above can dramatically improve the quality of Förster resonance energy transfer (FRET) measurements. Our approach simultaneously accounts for both the bleedthrough and the unknown background contribution, can provide an unbiased and background-free multi-parameter analysis of FRET efficiency without the need for spectral calibration and displays a much higher photon yield.

In Supplementary Fig. 17 we show how the Phasor S-FLIM analysis of four mCerulean-mVenus FRET constructs[28,29] eliminates unwanted background contribution as well as spectral bleedthrough and how, at the same time, it provides approximately a three times higher number of photons for each of the fluorophores with respect to filter-based methods (Supplementary Figs. 20 and 21). Since Phasor S-FLIM allows for the simultaneous acquisition of lifetime information from the unmixed donor and acceptor emissions, the resulting photon amount is up to 22 times higher for high FRET cases (VCVV) and six times higher for low FRET cases (C32V) compared with filter-based donor quenching FLIM experiments.

To demonstrate the robustness of Phasor S-FLIM to background contributions, we imaged 28 cells expressing the FRET standard C32V with varying expression levels, which we quantified as the average number of photons per pixel in the unmixed mCerulean channel. As shown in Fig. 3b, Phasor S-FLIM returns the same FRET efficiency regardless of the expression level and with a narrow distribution, whereas FLIM displays a broader distribution that is skewed at low expression levels due to the increased contribution of autofluorescent species (Fig. 3c).

The possibility to apply Phasor S-FLIM unmixing to weak FRET signals is particularly important in the case of biosensors. Since biosensors are typically designed to express fluorophores linked to functional molecules (in this case histone H3 and HP1), their overexpression is undesirable since it could cause physiological changes in the cell. Low expression, however, means also a weaker signal and more interference from autofluorescence that is present in the cell, as we showed in Fig. 3a–c. Typical sources for autofluorescence in the visible range for two-dimensional (2D) cell cultures are reduced nicotinamide adenine dinucleotide and flavins, such as flavin adenine dinucleotide, which have large excitation and absorption spectra, making them almost ubiquitous if the fluorescence signal is weak. To worsen the effect of these autofluorescent species, both molecules display multi-exponential decays with contributions varying from cell to cell, dramatically increasing the number of parameters to be taken into account, if we were to rely on a fitting method.

Most biosensors consist of either one or two functional proteins linked to a FRET pair. Changes in FRET efficiency are used as readouts to report on structural changes or binding events of interest. In Fig. 3d–g, we show an example of Phasor S-FLIM analysis of a chromatin compaction biosensor, described elsewhere[30]. Briefly, the H3Kme3 biosensor is a construct of histone H3, enhanced cyan fluorescent protein (ECFP), Heterochromatic Protein 1 (HP1) and YPet. HP1 is responsible for the methylation of lysine 9 of the H3, which is a posttranslational modification known to induce heterochromatin formation, while ECFP and YPet are the FRET pair. In Fig. 3d–g we show cells transfected with the chromatin compaction biosensor (H3Kme3) and in hypo-osmolar or hyper-osmolar conditions to induce chromatin decompaction and compaction, respectively[31]. Phasor S-FLIM allows to compute the FRET efficiency with a four to five times increased number of photons compared to FLIM, which results in much sharper images (Fig. 3e) and distributions (Fig. 3f,g), revealing small differences in FRET efficiency at the single cell level.

Photophysical characterization of solvatochromic probes in living cells: Laurdan and Nile Red.

A further application that greatly benefits from Phasor S-FLIM is the analysis of solvatochromic probes in living cells, such as Laurdan and Nile Red, which are widely used in flow cytometry and for the analysis of membrane composition and fluidity. In the following, we will show examples of these two polarity probes that display distinct photophysical properties[25,26,32,33] and we will show how the Phasor S-FLIM approach is capable of extensively characterizing their behavior in different cellular compartments.

Laurdan[34,35] (6-dodecanoyl-*N*,*N*-dimethyl-2-naphthylamine) is a polarity-sensitive dye originally synthesized by Weber and extensively characterized from both a spectral and time-resolved point of view[36,37] and used to characterize difference in membrane fluidity. Nile Red[38,39] (9-diethylamino-5-benzo[a]phenoxazinone) is another polarity-sensitive dye suitable for live cell imaging with an affinity for lipid droplets and membranes in cells.

In Fig. 4 we show the RGB images of cells stained with Laurdan (Fig. 4a) and Nile Red (Fig. 4b), obtained by combining the fluorescence signal from the spectral channels. A difference in color between lipid droplets (violet-blue in Fig. 4a and yellow in Fig.

4b) and internal membranes (green in Fig. 4a and orange in Fig. 4b) is clearly visible. A parameter used to characterize Laurdan's spectral emission is the so-called generalized polarization[36,40,41] (GP) computed from the intensity in a blue-shifted spectral window I_B (for example, 436 to 490 nm) and a red-shifted spectral window I_R (for example, 490 to 542 nm) as $GP = \frac{I_B - I_R}{I_B + I_R}$. A high value of GP means a lower polarity of the environment, therefore, for the membranes, a lower fluidity.

A pixel-resolved image of GP values is shown in Fig. 4a,b (right), in which three general regions can be appreciated: lipid droplets (red pixels, circle), high-GP membranes (yellow pixels, diamond) and low-GP membranes (green pixels, triangle). We performed a k-means clustering based image segmentation and cumulated the photons detected in these regions before performing the Phasor S-FLIM analysis, the results of which are shown in Fig. 4c–j. From the TRANES (Fig. 4c) we can appreciate a spectral redshift, which stems from the interaction of Laurdan with a more polar environment and shows higher polarity (higher fluidity) of the internal membranes compared to the lipid droplets.

Similarly, the Nile Red (Fig. 4b) staining shows a spectral redshift when considering lipid droplets (red pixels, circle) or internal membranes (green pixels, diamond), which have been segmented with a similar k-means clustering based approach. Here, the spectral windows used to compute the GP are 568–618 nm for I_B and 618–670 nm for I_G.

The advantages of Phasor S-FLIM analysis can be better appreciated by observing the τ- and λ phasors of the two solvatochromic probes in the segmented regions described above. In Fig. 4i,j, for instance, we observe that Laurdan λ phasors position as a function of time shifts (in the ns range) following a curved trajectory (Fig. 4i), whereas Nile Red follows a linear trajectory (Fig. 4j). Such behavior is expected since the photophysics of Laurdan is known to undergo a continuous spectral shift while Nile Red can be modeled as a two-state system. The same trend can be observed for the τ phasors (Fig. 4f,g). The capability of Phasor S-FLIM to unravel the precise photophysical behavior of a solvatochromic probe in living cells is an invaluable tool for the characterization of new solvatochromic dyes targeting the cellular environment.

As for the Nile Red analysis, we showed it can be described with a two-state model in both the τ and λ phasors. This means we can apply our Phasor S-FLIM unmixing algorithm described above to unmix the two spectral contributions of Nile Red and map their lifetime throughout the image. This property will be exploited in the following section.

Highly multiplexed FLIM analysis of biophysical properties: tumor spheroids.

FLIM is becoming increasingly important for addressing biological questions, for instance by exploiting fluorescent dyes that can probe the environment properties by changing their fluorescence lifetime or by analyzing the autofluorescence lifetime signature for metabolic studies. However, acquiring multiplexed FLIM experiments is still a very challenging task to perform and often achieved by exploiting a broad spectral range[42,43], which largely limits the combinations and number of dyes and fluorophores that can be used at the same time. Here, we show how Phasor S-FLIM can perform four-color FLIM imaging simultaneously

with a single excitation wavelength on tumor spheroids using a spectral window of only 170 nm.

Tumor spheroids represent a widely used three-dimensional model to study the spatial and functional heterogeneity of cellular subpopulations in avascular solid tumors[44,45]. Even when grown from a single cell line, different cells in tumor spheroids can display a huge array of characteristics, ranging from metabolic state[46], mitochondria membrane potential[47], cytoskeletal organization[48] and lipid metabolism[49], among others. Given the enormous variety of properties and their spatial distribution, it is extremely challenging to address them all in a single, parallel acquisition.

In Fig. 5, we show a spheroid grown from a human breast cancer cell line (MDA-MB231) labeled with JC-1 and Nile Red. JC-1 is a fluorescent lipophilic, cationic probe with a green emission spectrum that can enter the mitochondria. In active (high membrane potential) mitochondria, the probe accumulates forming J aggregates[50], which displays an orange emission spectrum. Nile Red has been shown in the previous paragraph that can be approximated to a two-spectra system to probe lipid organization and properties.

The four spectra completely overlap and, even with the single dyes, the two spectral emissions are intertwined, making it harder to obtain the pure spectral signatures of the dyes. Therefore, we applied the Phasor S-FLIM unmixing algorithm first to obtain the pure spectra of the single components from spheroids labeled with only JC-1 and only Nile Red. The unmixing process and the parameters obtained are schematized in Fig. 5a. Once we obtained the pure spectra, we could compute the first and second harmonics of their phasor transformation [51] (Supplementary Information) to unmix the four FLIM images (Fig. 5c) that compose the image ($L_{\mathrm{JC1},1}$, $L_{\mathrm{JC1},2}$, $L_{\mathrm{NR},1}$, $L_{\mathrm{NR},2}$) as well as the total intensity for every spectral component ($S_{\mathrm{JC1},1}$, $S_{\mathrm{JC1},2}$, $S_{\mathrm{NR},1}$, $S_{\mathrm{NR},2}$) from which we can calculate the spectral GP for the two probes, defined as $\mathrm{GP}_{\lambda,\mathrm{JC1}} = \frac{S_{\mathrm{JCl},1} - S_{\mathrm{JCl},2}}{S_{\mathrm{JCl},1} + S_{\mathrm{JCl},2}}$ and $\mathrm{GP}_{\lambda,\mathrm{NR}} = \frac{S_{\mathrm{NR},1} - S_{\mathrm{NR},2}}{S_{\mathrm{NR},1} + S_{\mathrm{NR},2}}$. L and S lifetime and spectral images, respectively, whereas the first subscript refers to the probe (JC1 for JC – 1 and NR for Nile Red) and the second subscript refers to the two spectral emissions (1 being the emission spectrum with the lower average emission wavelength). The unmixing procedure did not affect or bias the lifetime of the components, as shown in Supplementary Fig. 23.

Our multiplexed FLIM analysis yields a series of biophysical properties of interest, such as the lipid droplet concentration (Fig. 5d, shown as $\mathrm{GP}_{\lambda,\mathrm{NR}}$, high values corresponding to high concentration), the mitochondrial activity (Fig. 5e, shown as negative $\mathrm{GP}_{\lambda,\mathrm{JC1}}$, high values corresponding to high activity), the lipid order (Fig. 5f, from $L_{1,NR}$, shown as $1 - g^{(\tau)}$, high values corresponding to high order) and the hydrophobicity (Fig. 5g, from $L_{2,\mathrm{NR}}$, shown as $1 - g^{(\tau)}$, high values corresponding to high hydrophobicity).

This wealth of information allows us to appreciate different cellular populations, determine their spatial distribution and unravel their role in tumor organization, growth and metastasis. The properties we observed are in line with what was previously reported by other groups[52–56], and these properties are measured simultaneously at a cellular resolution in

living spheroids. The capability of obtaining multiplexed FLIM information in parallel using a single excitation wavelength has far-reaching applications in many areas of biological and biomedical research.

Discussion

We presented a combination of a new electronics design for multichannel lifetime acquisition and a powerful phasor-based analysis and unmixing algorithm for S-FLIM datasets that work in synergy to provide unbiased, background-free and photon-efficient analysis of hyperspectral lifetime measurements. The frame rate and optical resolution of the Phasor S-FLIM approach are limited only by the microscopy setup used, the data can be processed in real time, it can withstand photon fluxes of hundreds of MHz, corresponding to a photon flux a thousand times higher than the image shown in Fig. 2e, and it provides accurate results even with very low photon fluxes. Phasor S-FLIM is capable of delivering FLIM analysis with bias reduced by an order of magnitude, with higher precision and at a three to six orders of magnitude faster computational time, allowing the real-time analysis of S-FLIM data and opening the doors to highly parallel systems.

We demonstrated the applicability of Phasor S-FLIM with a series of challenging applications such as blind spectral and lifetime unmixing of unknown species in simulations, in solution and in both live and fixed cells. We demonstrated unbiased FRET analysis with up to an order of magnitude higher photon yield and background-free, high-precision determination of FRET efficiency from FRET standards and biosensors, as well as the photophysical characterization of solvatochromic probes in different compartments in living cell. The information obtained from these experiments allowed for simultaneous four-color FLIM imaging with a single excitation wavelength in living tumor spheroids, which yielded a variety of biophysical properties that ultimately lead to the direct visualization and quantification of cellular subpopulations with diverse biophysical signature.

Phasor S-FLIM pushes further the limits of fluorescence microscopy for the analysis of biological and biomedical specimens. In the era of big data, we strive to satisfy the ever-growing need for smart, photon-efficient technology and fast, precise computation that, we believe, will change the model of the way (S-)FLIM data are acquired and processed.

Online content

Any methods, additional references, Nature Research reporting summaries, source data, extended data, supplementary information, acknowledgements, peer review information; details of author contributions and competing interests; and statements of data and code availability are available at https://doi.org/10.1038/s41592-021-01108-4.

Methods

Microscopy.

All data were acquired with a custom-built microscope described in the Supplementary Information. The solution measurements and cells acquired for the FRET and Laurdan

experiments were acquired with 405 nm excitation light and a 410-nm long pass dichroic mirror (Semrock) whereas measurements for the Nile Red and tumor spheroids experiments were performed with a 488-nm excitation light and a 500-nm long pass dichroic mirror (Semrock). A Nikon ×100/1.45 numerical aperture (NA) Oil objective was used for the Laurdan and Nile Red experiments and the measurements in solutions, an Olympus PlanApo N ×60/1.45 NA Oil objective was used for all other cells experiments and an Olympus UPlanSApo ×20/0.75 NA air objective was used for imaging the tumor spheroids.

Cell culture and transient transfection.

CHO-cells were cultured in low glucose medium (Ham's F-12K Medium Kaighn's modification, Gibco, ThermoFisher Scientific), supplemented with 10% v/v fetal bovine serum (heat inactivated FBS, GenClone) and 1% v/v penicillin/streptomycin solution 100× (10,000 units of penicillin and 10 mg ml^{-1} streptomycin in 0.85% saline solution, GenClone), in a 37 °C and 5% CO_2 incubator.

MDA-MB231 cells were cultured in DMEM medium (DMEM, high glucose, with l-glutamine, GenClone), supplemented with 10% v/v FBS (heat inactivated FBS, GenClone) and 1% v/v penicillin/streptomycin solution 100x (10,000 units of penicillin and 10 mg ml^{-1} streptomycin in 0.85% saline solution, GenClone), in a 37 °C and 5% CO_2 incubator.

One day before transfection, MDA-MB231 cells were seeded in an eight-well chambered coverglass (Thermo Scientific, Nunc Lab-Tek), previously coated with 2 μg ml^{-1} fibronectin in Dulbecco's phosphate buffer solution (fibronectin human plasma 0.1% solution, Sigma-Aldrich; DPBS 1x without Ca, Mg, Phenol Red, GenClone). Transfections were performed with Lipofectamine 3000 (Invitrogen, ThermoFisher Scientific) diluted in Opti-MEM I reduced-serum medium (Gibco, ThermoFisher Scientific), according to the manufacturer's instructions. Approximately 1 d after transfection, Opti-MEM medium was substituted with culture medium (DMEM medium supplemented with 10% v/v FBS and 1% v/v penicillin/streptomycin solution 100x). The following FRET standard plasmids, used for transfections, were a gift from S. Vogel: C5V (Addgene plasmid no. 26394), C32V (Addgene plasmid no. 26396), mVenus N1 (Addgene plasmid no. 27793), mCerulean N1 (Addgene plasmid no. 27795), VCV (Addgene plasmid no. 27788) and VCVV (Addgene plasmid no. 27789). pCAG-CFP was a gift from C. Cepko (Addgene plasmid no. 11179). YPet-N1 was a gift from P. Daugherty and M. Davidson (Addgene plasmid no. 54637). THe H3K9me3 biosensor was a gift from Y. Wang (Addgene plasmid no. 120802). For each plasmid, bacterial growth was spread on Luria-Bertani medium (LB) agar plates with the appropriate antibiotic; single colonies were inoculated in a liquid culture of LB and antibiotic and placed in a shaking incubator (37 °C, 270 r.p.m.) overnight. Plasmid DNA was then purified from bacterial growth using a mini-prep kit (QIAprep Spin Miniprep Kit, QIAGEN) and concentration was verified with Nanodrop2000 (ThermoFisher Scientific).

MDA-MB231 spheroids were formed starting from a culture of 20,000 cells per spheroid mixed with their medium and a 2% Matrigel (Corning Matrigel Matrix) solution in 96-well round-bottom plates (Corning Costar Ultra-Low Attachment Multiple Well Plate). After a brief centrifugation (5 min at 1,000 r.p.m.) and 3 d of incubation (37 °C, 5% CO_2), the spheroids were transferred in eight-well chambers (Nunc Lab-Tek Chambered Coverglass)

and embedded in a 3.0 mg ml^{-1} collagen Type-1 gel matrix (Corning Collagen I, Rat Tail, 100 mg). Media and dyes were added on top after collagen polymerization and incubated at 37 °C and 5% CO_2 before imaging.

MDA-MB231 tumor spheroids.

MDA-MB231 cells were cultured in DMEM medium (DMEM, high glucose, with l-glutamine, GenClone), supplemented with 10% v/v heat inactivated FBS (GenClone) and 1% v/v penicillin/streptomycin solution 100x (10,000 units of penicillin and 10 mg ml^{-1} streptomycin in 0.85% saline solution, GenClone), in a 37 °C and 5% CO_2 incubator. MDA-MB231 spheroids were formed starting from a culture of 20,000 cells per spheroid mixed with their medium and a 2% Matrigel (Corning Matrigel Matrix) solution in 96-well round-bottom plates (Corning Costar Ultra-Low Attachment Multiple Well Plate). After a brief centrifugation (5 min at 1,000 r.p.m.) and 3 d of incubation (37 °C, 5% CO_2), the spheroids were transferred in eight-well chambers (Nunc Lab-Tek Chambered Coverglass) and embedded in a 3.0 mg ml^{-1} collagen Type-1 gel matrix (Corning Collagen I, Rat Tail, 100 mg). Media and dyes were added on top after collagen polymerization and incubated at 37 °C and 5% CO_2 before imaging.

Solutions, fluorescent labeling and treatments.

The set of solutions used for calibration was prepared at a concentration of 7 μM in PBS pH 7.4 and consists in a solution of Alexa 405 (Thermofisher Scientific), fluorescein (Thermofisher Scientific) and ATTO490LS (ATTO-tec). The mixture of three solutions is composed by a mixture of Alexa 405 at 400 nM, SeTau 405 (Seta Biomedicals) at 2 μM and ATTO 490 LS at 8 μM in PBS pH 7.4. Alexa 405 and SeTau 405 display an absorption maximum at 405 nm, and ATTO 490 LS absorbs at 38% of its absorption maximum. The concentrations were adjusted to have a photon amount of the same order of magnitude from the three emission spectra (67, 16 and 17%, respectively).

Live cells in Fig. 2a were stained with 1:5,000 ViaFluor 488 (Biotium), 200 nM MitoTracker Orange CMTMRos (Thermofisher) and 1 μM LysoTracker DND-99 Red (Thermofisher), incubated 30 min and washed twice before imaging. Dyes were diluted to have less than 0.1% DMSO in the medium.

Immunostaining samples were prepared as follows. One day before immunostaining, MDA-MB231 cells were seeded in eight-well chambered coverglass (Thermo Scientific, Nunc Lab-Tek), previously coated with 2 μg ml^{-1} fibronectin in DPBS (fibronectin human plasma 0.1% solution, Sigma-Aldrich; DPBS 1x without Ca, Mg, Phenol Red, GenClone). Cells were washed twice with warm DPBS 1x and fixed with paraformaldehyde 4% in PBS (Ready-to-Use Fixative, Biotium) for 15 min at room temperature. Cells were washed with DPBS 1x, permeabilized with 0.1% Triton X-100 in DPBS 1x for 15 min at room temperature and washed with DPBS 1x. The samples were incubated for 1 h at room temperature with a blocking solution of 0.1% Triton X-100 + 1% BSA (albumin from bovine serum, Sigma) + 10% Normal Goat Serum (Abcam, ab7481) in DPBS 1x, then incubated in the dark for 1 h at room temperature with Phalloidin-Alexa594 (Thermofisher) diluted 1:400 in DPBS 1x + 1% BSA. After washing with DPBS 1x,

the samples were incubated overnight at 4 °C with anti-TOMM20-Alexa555 (Abcam, ab221292) antibody diluted in the blocking buffer 1:250. After washing with DPBS1X, samples were incubated with NucSpot 488 (Biotium) diluted 1:30,000, mounted with Fluoromount (Sigma) mounting medium and preserved in the dark at 4 °C.

For the solvatochromic dyes staining, stock solutions of Laurdan (Toronto Research Chemicals) and Nile Red (Thermofisher Scientific) at 30 mM in DMSO were prepared and diluted 1:10,000 at a final concentration of 3 μM in cellular media, left incubating in a 37 °C and 5% CO_2 incubator for 30 min. Tumor spheroids were labeled with 3 μM Nile Red and 2 μM JC-1 diluted in cellular media. JC-1 was diluted 1:1,000 from a 2 mM stock solution in DMSO.

Hypo-osmolar medium was prepared by diluting DMEM 1:1 in milli-Q water, reducing the osmolarity by half with respect to DMEM. Hyper-osmolar medium was prepared by diluting PBS 10× 1:10 in DMEM, increasing by osmolarity by approximately a factor of two with respect to DMEM. Cells were plated as described above, warm hypo- or hyper-osmolar medium was substituted to culture medium and cells were imaged within 1 h.

Simulations and computer code.

All simulations were performed in MATLAB 2019b. Data for Fig. 1b–d were simulated as follows: a variable number of photons were drawn from a single exponential probability distribution corresponding to a lifetime of 0.5 ns, of which a histogram was computed to model a lifetime decay. To mimic a realistic measurement, the histogram was calculated over five times the actual period and the photon arrived in each of the five periods were cumulated together. This is particularly important when simulating long lifetimes or IRF convolution, in which photons may arrive in periods adjacent to the one in which the fluorescence was excited. For fitting, the initial parameters (height and exponential constant) were initialized to the true values. A set of 10,000 realizations was simulated for every number of photons and the error was computed as the standard deviation of the resulting values of lifetime, whereas the bias was computed as the average of the resulting values of lifetime minus the simulated value.

Data for Fig. 1e–j were simulated as follows: a fixed number of photons (1,000) were drawn from a single exponential probability distribution corresponding to a lifetime of 2.5 ns and spread following a Gaussian distribution centered in 0 with variable FWHM to mimic the instrument IRF. A constant background affected by Poisson noise with variable average number of photons was also added.

For the speed comparison, pure exponentials with a lifetime of 1 ns were simulated and fitted with the MATLAB function ‘fminsearch’. The same dataset was also transformed into phasors and the lifetime was obtained as $\tau = \frac{s}{\omega g}$ (see Supplementary Information for further details). The average computational time and standard deviation was computed from a set of 100 realizations with a varying number of iterations. For the data in Fig. 1e–j the median of 1,000 realizations was considered, the curves were fitted with a single exponential convolved with a known Gaussian IRF and affected by a constant background.

The S-FLIM datasets simulated in Supplementary Fig. 9 were simulated as follows: three Gaussian spectra with center at 480, 540 and 620 nm were simulated and standard deviations of 30, 35 and 45 nm were simulated. Each spectrum was simulated with a different lifetime: spectrum one was a combination of 8 and 0.2 ns, spectrum two was a combination of 4 and 1 ns whereas spectrum three was a pure exponential with lifetime 2.5 ns. The total number of photons for the dataset was set at 500,000 and noise was added with the PoissonNoise function in MATLAB. We simulated 100 realizations, each of which was analyzed and unmixed by the Phasor S-FLIM blind unmixing algorithm described in the main text.

Colormaps in Fig. 5 were obtained by the superjet function: A. Vallmitjana Lees (2020). Superjet (https://www.mathworks.com/matlabcentral/fileexchange/74715-superjet) RGB images were reconstructed by transforming the image relative to each spectral channel to an RGB image and successively combining them in a single RGB image. Wavelength to RGB conversion was performed using the function SpectrumRGB (J. Mather (2020). Spectral and XYZ Color Functions MATLAB Central File Exchange).

Phasor S-FLIM.

Phasor S-FLIM analysis was performed on the entire image (solution measurements) or on a thresholded image (cells and spheroids) with a user-defined threshold. No spectral correction was applied to any dataset in the paper.

The number of photons in Fig. 2d–f was reduced by considering only a fraction of the photons detected in each pixel from 10% (0.6 photons per pixel per dye) to 100% (11.3 photons per pixel per dye, Fig. 2c).

FRET efficiency in Fig. 3 for Phasor S-FLIM was calculated as an average between the FRET efficiency image obtained by the lifetime of mCerulean after unmixing and from the spectral FRET computed from the intensity of the mCerulean and mVenus unmixed channels. We report the lifetimes of mCerulean and ECFP to be multi-exponential, as also reported elsewhere[57,58]; therefore, their lifetime for the FRET calculation was fixed at 3.3 and 3.0 ns, respectively, to be consistent with the literature[29,59].

Regions in Fig. 4a,b were segmented by *k*-means clustering using GP and intensity information with seven clusters. A user-defined number of clusters was merged together for each of the considered regions. TRES from pixels assigned to the same cluster were combined to perform the analysis shown in Fig. 4c–j, a representative region is shown by the markers.

Pure components for Nile Red and JC-1 in Fig. 5 were obtained by Phasor S-FLIM unmixing of spheroids labeled with the single dyes, the spectra were then stored and their first and second harmonic phasors were used to unmix the sample labeled with both dyes.

Supplementary Material

Refer to Web version on PubMed Central for supplementary material.

Acknowledgements

We thank F. Palomba, A. Vallmitjana Lees, C. Gohlke and A. Dvornikov for the useful discussion and D. Jameson for his input on the paper. This work was supported by grant no. NIH P41-GM103540.

Data availability

The data that support the findings of this study are available from the corresponding author upon reasonable request. Source data are provided with this paper.

References

1. Becker W, Bergmann A, Biscotti GL & Rueck A Advanced time-correlated single photopy and imaging in biomedical systems. In Proc. Commercial and Biomedical Applications of Ultrafast Lasers IV: Lasers and Applications in Science and Engineering Conference (eds. Neev J et al.) (SPIE, 2004); 10.1117/12.529143
2. Owen DM et al. Excitation-resolved hyperspectral fluorescence lifetime imaging using a UV-extended supercontinuum source. Opt. Lett. 32, 3408–3410 (2007). [PubMed: 18059949]
3. Fereidouni F, Reitsma K & Gerritsen HC High speed multispectral fluorescence lifetime imaging. Opt. Express 21, 11769–11782 (2013). [PubMed: 23736399]
4. Borlinghaus R & Kuschel L Spectral fluorescence lifetime imaging microscopy: new dimensions with Leica TCS SP5. Nat. Methods 3, 868 (2006).
5. König K (ed.) Multiphoton Microscopy and Fluorescence Lifetime Imaging: Applications in Biology and Medicine (De Gruyter, 2018); 10.1515/9783110429985
6. Yan L, Rueden CT, White JG & Eliceiri KW Applications of combined spectral lifetime microscopy for biology. BioTechniques 41, 249, 251, 253 (2006).
7. Rueck AC, Lorenz S, Hauser C, Mosch S & Kalinina S Multiwavelength FLIM: new concept for fluorescence diagnosis. In Proc. Multiphoton Microscopy in the Biomedical Sciences XII (ed. König K) (SPIE, 2012); 10.1117/12.906620
8. Levenson RM, Lynch DT, Kobayashi H, Backer JM & Backer MV Multiplexing with multispectral imaging: from mice to microscopy. ILAR J. 49, 78–88 (2008). [PubMed: 18172335]
9. Gratton E Fluorescence lifetime imaging for the two-photon microscope: time-domain and frequency-domain methods. J. Biomed. Opt. 10.1117/1.1586704 (2003).
10. Jameson DM, Gratton E & Hall RD The measurement and analysis of heterogeneous emissions by multifrequency phase and modulation fluorometry. Appl. Spectrosc. Rev. 10.1080/05704928408081716 (1984).
11. Lou J et al. Phasor histone FLIM-FRET microscopy quantifies spatiotemporal rearrangement of chromatin architecture during the DNA damage response. Proc. Natl Acad. Sci. USA 116, 7323–7332 (2019). [PubMed: 30918123]
12. Digman MA, Caiolfa VR, Zamai M & Gratton E The phasor approach to fluorescence lifetime imaging analysis. Biophys. J. 94, 14–16 (2008). [PubMed: 17827229]
13. Scipioni L, Gratton E, Diaspro A & Lanzanò L Phasor analysis of local ICS detects heterogeneity in size and number of intracellular vesicles. Biophys. J. 111, 619S (2016).
14. Ranjit S, Malacrida L, Jameson DM & Gratton E Fit-free analysis of fluorescence lifetime imaging data using the phasor approach. Nat. Protoc. 13, 1979–2004 (2018). [PubMed: 30190551]
15. Sarmento MJ et al. Exploiting the tunability of stimulated emission depletion microscopy for super-resolution imaging of nuclear structures. Nat. Commun. 9, 3415 (2018). [PubMed: 30143630]
16. Hanley QS Spectrally resolved fluorescent lifetime imaging. J. R. Soc. Interface 6, S83–S92 (2009).
17. Cutrale F, Salih A & Gratton E Spectral phasor approach for fingerprinting of photo-activatable fluorescent proteins Dronpa, Kaede and KikGR. Methods Appl. Fluoresc. 1, 35001 (2013). [PubMed: 24040513]

18. Cutrale F et al. Hyperspectral phasor analysis enables multiplexed 5D in vivo imaging. Nat. Methods 14, 149–152 (2017). [PubMed: 28068315]
19. Fereidouni F, Bader AN & Gerritsen HC Spectral phasor analysis allows rapid and reliable unmixing of fluorescence microscopy spectral images. Opt. Express 20, 12729–12741 (2012). [PubMed: 22714302]
20. Ranjit S, Malacrida L & Gratton E Differences between FLIM phasor analyses for data collected with the Becker and Hickl SPC830 card and with the FLIMbox card. Microsc. Res. Tech. 81, 980–989 (2018). [PubMed: 30295346]
21. Ma WK et al. A signal processing perspective on hyperspectral unmixing: Insights from remote sensing. IEEE Signal Process Mag. 10.1109/MSP.2013.2279731 (2014).
22. Keshava N A survey of spectral unmixing algorithms. Linc. Lab. J. 14, 55–78 (2003).
23. McRae TD, Oleksyn D, Miller J & Gao YR Robust blind spectral unmixing for fluorescence microscopy using unsupervised learning. PLoS ONE 14, e0225410 (2019). [PubMed: 31790435]
24. Neher RA et al. Blind source separation techniques for the decomposition of multiply labeled fluorescence images. Biophys. J. 96, 3791–3800 (2009). [PubMed: 19413985]
25. Medintz I & Hildebrandt N (eds.) FRET—Förster Resonance Energy Transfer: From Theory to Applications (Wiley, 2013); 10.1002/9783527656028
26. Gopich IV & Szabo A Theory of the energy transfer efficiency and fluorescence lifetime distribution in single-molecule FRET. Proc. Natl Acad. Sci. USA 109, 7747–7752 (2012). [PubMed: 22550169]
27. Vallmitjana A, Torrado B, Dvornikov A, Ranjit S & Gratton E Blind resolution of lifetime components in individual pixels of fluorescence lifetime images using the phasor approach. J. Phys. Chem. B 124, 10126–10137 (2020). [PubMed: 33140960]
28. Koushik SV, Blank PS & Vogel SS Anomalous surplus energy transfer observed with multiple FRET acceptors. PLoS ONE 4, e8031 (2009). [PubMed: 19946626]
29. Koushik SV, Chen H, Thaler C, Puhl HL & Vogel SS Cerulean, venus, and venusY67C FRET reference standards. Biophys. J. 91, L99–L101 (2006). [PubMed: 17040988]
30. Peng Q et al. Coordinated histone modifications and chromatin reorganization in a single cell revealed by FRET biosensors. Proc. Natl Acad. Sci. USA 115, E11681–E11690 (2018). [PubMed: 30478057]
31. Pelicci S, Diaspro A & Lanzanò L Chromatin nanoscale compaction in live cells visualized by acceptor-to-donor ratio corrected Förster resonance energy transfer between DNA dyes. J. Biophotonics 12, e201900164 (2019). [PubMed: 31365191]
32. Algar WR, Hildebrandt N, Vogel SS & Medintz IL FRET as a biomolecular research tool—understanding its potential while avoiding pitfalls. Nat. Methods 16, 815–829 (2019). [PubMed: 31471616]
33. Hellenkamp B et al. Precision and accuracy of single-molecule FRET measurements—a multi-laboratory benchmark study. Nat. Methods 15, 669–676 (2018). [PubMed: 30171252]
34. Bagatolli LA in Fluorescent Methods to Study Biological Membranes (eds. Mély Y & Duportail G) 3–35 (Springer, 2012).
35. Weber G & Farris FJ Synthesis and spectral properties of a hydrophobic fluorescent probe: 6-propionyl-2-(dimethylamino)naphthalene. Biochemistry 18, 3075–3078 (1979). [PubMed: 465454]
36. Parasassi T & Gratton E Membrane lipid domains and dynamics as detected by Laurdan fluorescence. J. Fluoresc. 5, 59–69 (1995). [PubMed: 24226612]
37. Parasassi T, Krasnowska EK, Bagatolli L & Gratton E Laurdan and prodan as polarity-sensitive fluorescent membrane probes. J. Fluoresc. 8, 365–373 (1998).
38. Swain J & Mishra AK Nile red fluorescence for quantitative monitoring of micropolarity and microviscosity of pluronic F127 in aqueous media. Photochem. Photobiol. Sci. 15, 1400–1407 (2016). [PubMed: 27714310]
39. Kreder R et al. Solvatochromic Nile Red probes with FRET quencher reveal lipid order heterogeneity in living and apoptotic cells. ACS Chem. Biol. 10, 1435–1442 (2015). [PubMed: 25710589]

40. Sanchez SA, Tricerri MA, Gunther G & Gratton E in Modern Research and Educational Topics in Microscopy (eds. Méndez-Vilas A & Díaz J) 1007–1014 (FORMATEX, 2007).
41. Sanchez SA, Tricerri MA & Gratton E Laurdan generalized polarization fluctuations measures membrane packing micro-heterogeneity in vivo. Proc. Natl Acad. Sci. USA 109, 7314–7319 (2012). [PubMed: 22529342]
42. Bückers J, Wildanger D, Vicidomini G, Kastrup L & Hell SW Simultaneous multi-lifetime multi-color STED imaging for colocalization analyses. Opt. Express 19, 3130–3143 (2011). [PubMed: 21369135]
43. Laviv T et al. Simultaneous dual-color fluorescence lifetime imaging with novel red-shifted fluorescent proteins. Nat. Methods 13, 989–992 (2016). [PubMed: 27798609]
44. Yamada KM & Cukierman E Modeling tissue morphogenesis and cancer in 3D. Cell 130, 601–610 (2007). [PubMed: 17719539]
45. Tevis KM, Colson YL & Grinstaff MW Embedded spheroids as models of the cancer microenvironment. Adv. Biosyst. 10.1002/adbi.201700083 (2017).
46. Ramanujan VK Quantitative imaging of morphometric and metabolic signatures reveals heterogeneity in drug response of three-dimensional mammary tumor spheroids. Mol. Imaging Biol. 21, 436–446 (2019). [PubMed: 30805885]
47. Avagliano A et al. Mitochondrial flexibility of breast cancers: a growth advantage and a therapeutic opportunity. Cells 8, 401 (2019). [PubMed: 31052256]
48. Smyrek I et al. E-cadherin, actin, microtubules and FAK dominate different spheroid formation phases and important elements of tissue integrity. Biol. Open 8, bio037051 (2019). [PubMed: 30578251]
49. Vidavsky N et al. Mapping and profiling lipid distribution in a 3D model of breast cancer progression. ACS Cent. Sci. 5, 768–780 (2019). [PubMed: 31139713]
50. Sivandzade F, Bhalerao A & Cucullo L Analysis of the mitochondrial membrane potential using the cationic JC-1 dye as a sensitive fluorescent probe. Bio Protoc. 9, e3128 (2019).
51. Vallmitjana A et al. Resolution of 4 components in the same pixel in FLIM images using the phasor approach. Methods Appl. Fluoresc. 8, 035001 (2020). [PubMed: 32235070]
52. Navarro-Tito N, Soto-Guzman A, Castro-Sanchez L, Martinez-Orozco R & Salazar EP Oleic acid promotes migration on MDA-MB-231 breast cancer cells through an arachidonic acid-dependent pathway. Int. J. Biochem. Cell Biol. 42, 306–317 (2010). [PubMed: 19931412]
53. Abramczyk H et al. The role of lipid droplets and adipocytes in cancer. Raman imaging of cell cultures: MCF10A, MCF7, and MDA-MB-231 compared to adipocytes in cancerous human breast tissue. Analyst 140, 2224–2235 (2015). [PubMed: 25730442]
54. Heerdt BG, Houston MA & Augenlicht LH The intrinsic mitochondrial membrane potential of colonic carcinoma cells is linked to the probability of tumor progression. Cancer Res. 10.1158/0008-5472.CAN-05-2444 (2005).
55. Reynolds DS et al. Breast cancer spheroids reveal a differential cancer stem cell response to chemotherapeutic treatment. Sci. Rep. 7, 10382 (2017). [PubMed: 28871147]
56. Szlasa W, Zendran I, Zalesińska A, Tarek M & Kulbacka J Lipid composition of the cancer cell membrane. J. Bioenerg. Biomembr. 52, 321–342 (2020). [PubMed: 32715369]
57. Kremers GJ, Goedhart J, Van Munster EB & Gadella TWJ Cyan and yellow super fluorescent proteins with improved brightness, protein folding, and FRET förster radius. Biochemistry 45, 6570–6580 (2006). [PubMed: 16716067]
58. Goedhart J et al. Bright cyan fluorescent protein variants identified by fluorescence lifetime screening. Nat. Methods 7, 137–139 (2010). [PubMed: 20081836]
59. Rizzo MA, Springer GH, Granada B & Piston DW An improved cyan fluorescent protein variant useful for FRET. Nat. Biotechnol. 22, 445–449 (2004). [PubMed: 14990965]

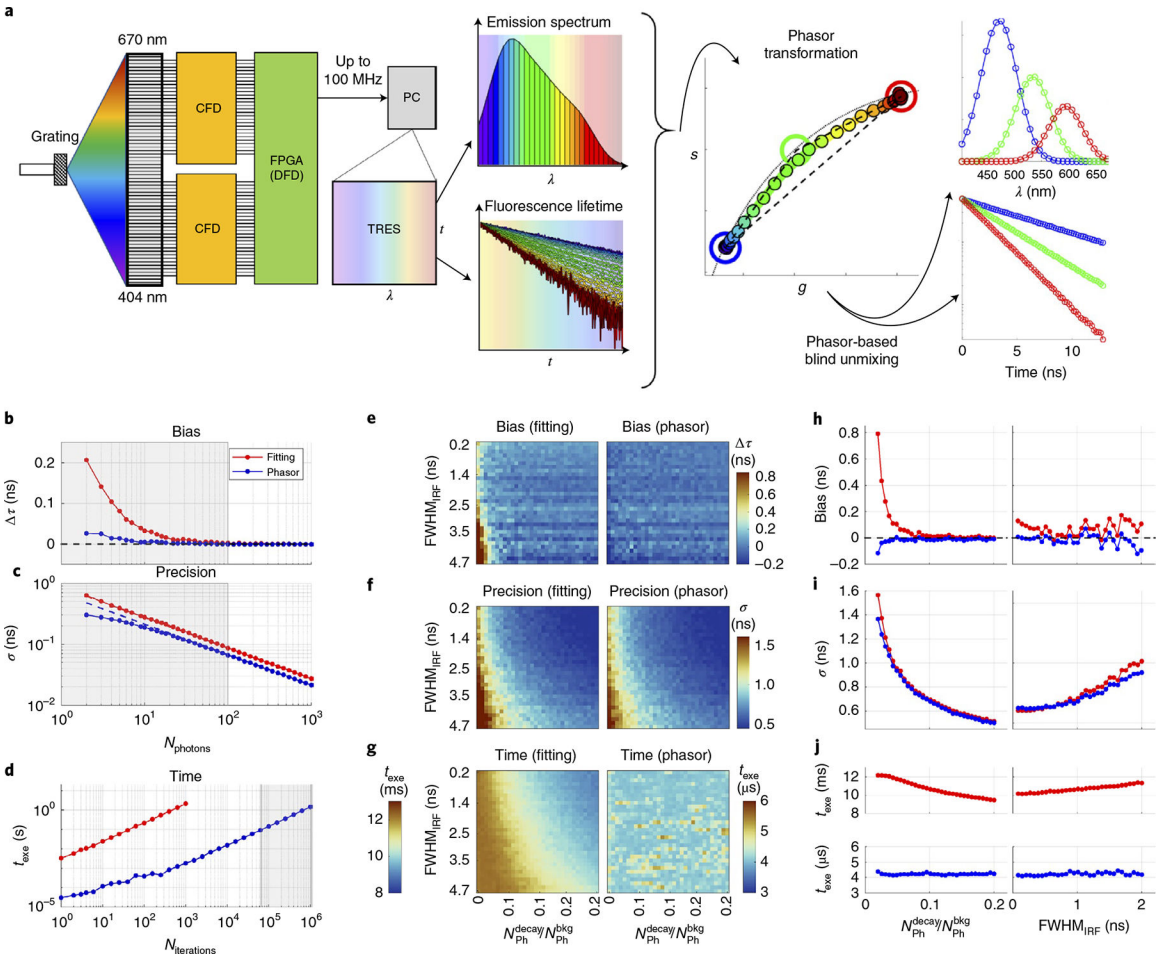

Fig. 1 |. Phasor S-FLIM workflow and robustness to noise of the phasor approach.

a, Schematic representation of the Phasor S-FLIM workflow. From left to right, fluorescence emission is chromatically separated by a diffraction grating and collected by a 32-channel PMT detector array, ranging from 404 to 670 nm. Single photon pulses are timed by two 16-channel constant fraction discriminators (CFDs) and their digital output is processed by an FPGA-based DFD architecture. Data are streamed via USB 3.0 to a computer for postprocessing and a 5D matrix (2D space, wavelength, time in nanoseconds, time in frames) is transformed to the phasor space and blindly unmixed to identify the pure spectral and lifetime components. **b**,**c**, Bias (**b**) and standard deviation (**c**) as a function of the number of photons used in the simulation of a 0.5 ns decay with varying number of photons. **d**, Execution time (exe) as a function of the number of points analyzed, numbers of iterations higher than 10^3 were not considered for the fitting due to the long execution time. Gray shaded areas correspond to an approximate range for a typical FLIM image, considering 2 to 100 photons per pixel (**b** and **c**) and a number of pixels ranging from 256 × 256 to 1,024 × 1,024 (**d**). Curves refer to phasor transformation (blue) and LMS fit (red). **e**–**g**, Bias (**e**), standard deviation (**f**) and execution time (**g**) as a function of the FWHM of the simulated Gaussian IRF and the SBR for phasor transformation (right) and LMS fit (left). Surfaces are obtained from 1,000 realizations of a 2.5 ns decay obtained from 1,000 photons. Average profiles for bias (**h**), standard deviation (**i**) and execution time (**j**) as a function of the FWHM

of the simulated Gaussian IRF (left) and the SBR (right) for phasor transformation (blue) and LMS fit (red). SBR is defined as the number of photons used to simulate the decay $N_{\mathrm{Ph}}^{\mathrm{delay}}$ over the number of photons used to simulate the background $N_{\mathrm{Ph}}^{\mathrm{bkg}}$.

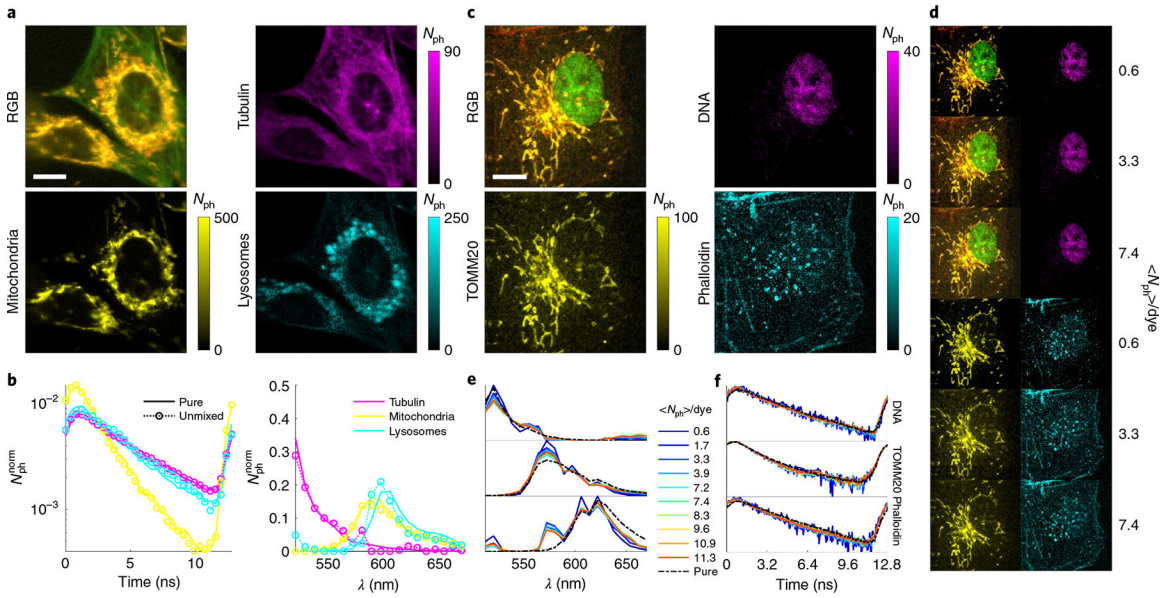

Fig. 2 |. Phasor S-FLIM spectral and lifetime blind unmixing of cellular samples.

a, RGB image, corresponding to approximately 30 photons per dye per pixel, and unmixed FLIM images of live cells labeled with ViaFluor 488 (tubulin, top right), MitoTracker Orange (mitochondria, bottom left) and LysoTracker Red (lysosomes, bottom right). A gamma correction is applied to the RGB image to make the tubulin and lysosome staining visible. **b**, Average lifetime (left) and spectra (right) for tubulin (green), mitochondria (yellow) and lysosomes (red) of the unmixed images shown in **a** (open circles) compared with pure components (solid lines). **c**, RGB image and unmixed FLIM images of a fixed cell labeled with NucSpot 488 (DNA, top right), anti-TOMM20/Alexa555 (mitochondria, bottom left) and Phalloidin/Alexa564 (actin, bottom right), corresponding to 11.3 photons per dye per pixel. **d**, RGB image and unmixed FLIM images of the same fixed cell depicted in **c** with reduced photon amount, stated on the right. **e**,**f**, Average spectra (**e**) and lifetime (**f**) obtained for DNA (top), mitochondria (center) and actin (bottom) with photon amount varying from 0.6 (purple) to 11.3 (orange) photons per dye per pixel, compared with pure components (black dash-dotted lines). All cells depicted are representative of three biological replicates yielding similar results. Scale bars, 10 μm.

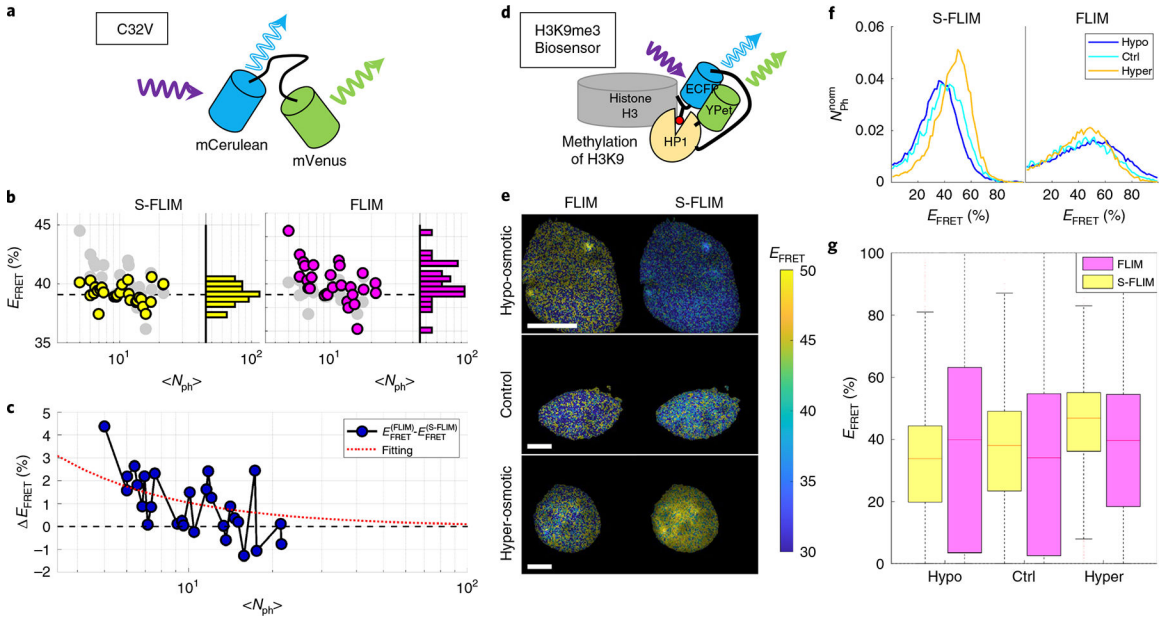

Fig. 3|. Phasor S-FLIM approach to FRET standards and biosensors.

a, Schematic representation of the C32V FRET standard. **b**, FRET efficiency as a function of the expression level (< N_{Ph} >, number of photons per pixel for the unmixed mCerulean) for Phasor S-FLIM (left, yellow and right, gray) and FLIM (left, gray and right, red). **c**, Difference in FRET efficiency between FLIM and Phasor S-FLIM as a function of the expression level (blue dots) and fitting (red dotted) with a function $f = \frac{A}{< N_{ph} >}$, where A is a constant scale factor. **d**, Schematic representation of the H3K9me3 chromatin compaction FRET biosensor. **e**, FRET images obtained by FLIM (left) and Phasor S-FLIM (right) for cells in hypo-osmotic medium (top), control (center) and cells on hyper-osmotic medium (bottom). **f**, Distribution of FRET efficiency obtained by Phasor S-FLIM (left) and FLIM (right) for the cells depicted in **e**. **g**, Box plots of FRET efficiency obtained by Phasor S-FLIM (yellow) and FLIM (pink) for the cells depicted in **e**. Median FRET efficiencies are 40.0% (hypo-osmotic), 34.1% (control) and 39.7% (hyper-osmotic) for FLIM and 33.8% (hypo-osmotic), 38.1% (control) and 46.8% (hyper-osmotic) for Phasor S-FLIM. In **g**, red lines represent the median, the edges of the box the 25th and 75th percentiles and the whiskers extend to the most extreme datapoints. The numbers of pixels analyzed for **f** and **g** are n = 15,029 (control), n = 16,402 (hyper-osmotic) and n = 41,847 (hypo-osmotic). The number of cells analyzed for **a–c** is 28, obtained from three biological replicates, while cells in **e** are representative of four biological replicates yielding similar results. Scale bars, 10 μm.

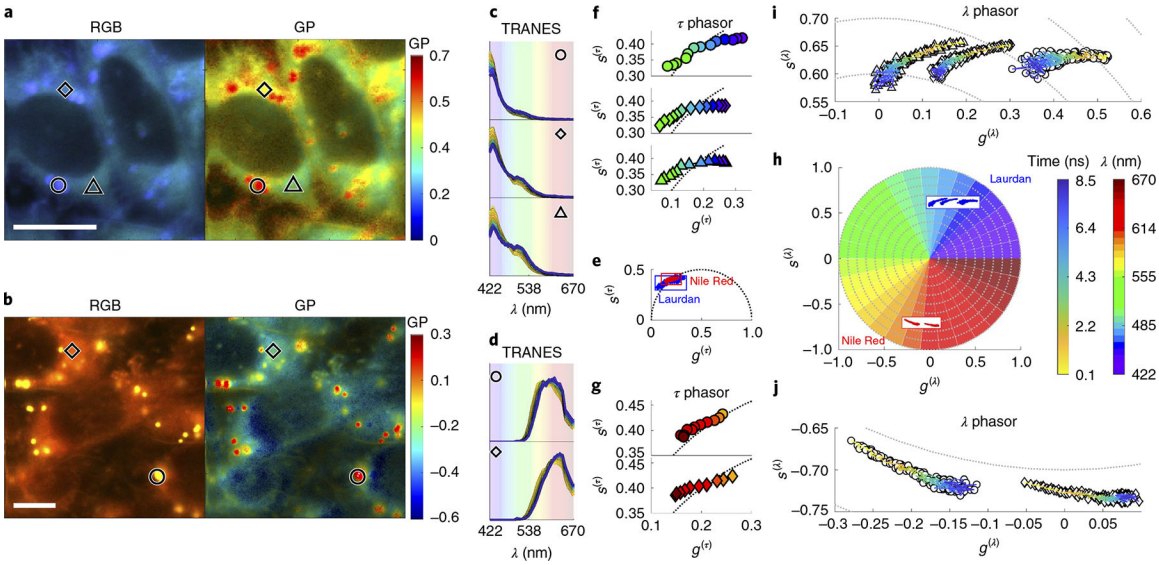

Fig. 4 |. Phasor S-FLIM characterization of solvatochromic probes in living cells.

a, RGB (left) and GP (right) images of cells labeled with Laurdan, symbols represent lipid droplets (circle), high-GP internal membranes (diamond) and low-GP internal membranes (circle). **b**, RGB (left) and GP (right) images of cells labeled with Nile Red, symbols represent lipid droplets (circle) and internal membranes (diamond). **c**,**d**,**f**,**g**,**i**,**j**, TRANES (**c**,**d**), τ phasor (**f**,**g**) and λ phasor (**i**,**j**) for Laurdan (**c**,**f**,**i**) and Nile Red (**d**,**g**,**j**) for the regions depicted in **a** and **b**, respectively. **e**,**h**, τ phasor plot (**e**) and λ phasor plot (**h**) showing the position of the Laurdan (blue) and Nile Red (red) regions. The parula (yellow to blue) colormap represents temporal evolution whereas the RGB colormap (purple to dark red) is an RGB representation of the central wavelength for the associated spectral channel. Cells in **a**,**b** are representative of three biological replicates yielding similar results. Scale bars, 10 μm.

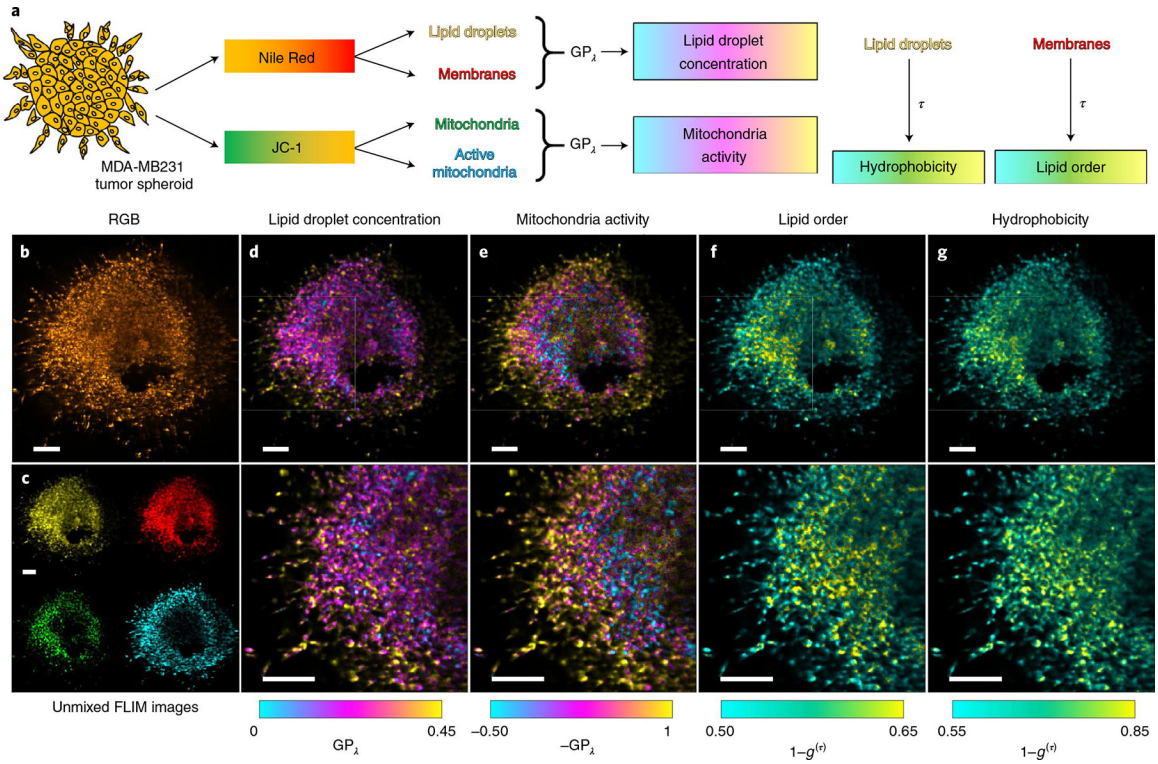

Fig. 5 |. Phasor S-FLIM single-cell physiological profiling of living tumor spheroids.

a, Schematic representation of the analysis pipeline. **b**, MDA-MB231 tumor spheroids are labeled with Nile Red and JC-1 as shown in the RGB image. Using the calibrated spectral signature of the dyes, four FLIM images are unmixed. **c**, The unmixed images are associated with lipid droplets (top left), internal membranes (top right), mitochondria (bottom left) and active mitochondria (bottom right). **d**,**e**, Average intensity images are combined to obtain GP_λ maps corresponding to lipid droplet concentration (**d**) and mitochondria activity (**e**). **f**,**g**, FLIM images of the Nile Red spectral emission are used to map lipid order of the internal membranes (**f**) and hydrophobicity of the lipid droplets (**g**). The spheroid depicted is representative of three biological replicates yielding similar results. Scale bars, 50 μm.